Three-dimensional dendrite-tip morphology at low undercooling

Alain Karma, Youngyih H. Lee, and Mathis Plapp
Physics Department and Center for Interdisciplinary Research on Complex Systems, Northeastern University, Boston, Massachusetts 02115
(Received 2 September 1999)

We investigate the three-dimensional morphology of the dendrite tip using the phase-field method. We find that, for low undercoolings, this morphology is ostensibly independent of anisotropy strength except for a localized shape distortion near the tip that only affects the value of the tip radius ρ [which is crudely approximated by $\rho \approx (1-\alpha)\rho_{Iv}$ where ρ_{Iv} is the Ivantsov tip radius of an isothermal paraboloid with the same tip velocity and α is the stiffness anisotropy]. The universal tip shape, which excludes this distortion, is well fitted by the form $z=-r^2/2+A_4 r^4 \cos 4\phi$ where $|z|$ is the distance from the tip and all lengths are scaled by ρ_{Iv}. This fit yields A_4 in the range $0.004-0.005$ in good quantitative agreement with the existing tip morphology measurements in succinonitrile [LaCombe *et al.*, Phys. Rev. E **52**, 2778 (1995)], which are reanalyzed here and found to be consistent with a single $\cos 4\phi$ mode nonaxisymmetric deviation from a paraboloid. Moreover, the fin shape away from the tip is well fitted by the power law $z=-a|x|^{5/3}$ with $a \approx 0.68$. Finally, the characterization of the operating state of the dendrite tip is revisited in the light of these results.

PACS number(s): 68.70.+w, 81.10.Aj, 64.70.Dv, 81.30.Fb

I. INTRODUCTION

The shape of crystal dendrites was first suggested by Papapetrou [1] to be parabolic, and slightly more than a decade later Ivantsov demonstrated [2] that a parabola (paraboloid) is an exact solution of the steady-state growth equations in two (three) dimensions when capillary effects are entirely neglected and the interface is isothermal. He derived the well-known relationship

$$\Delta = P_{Iv} \exp(P_{Iv}) \int_{P_{Iv}}^{\infty} ds \, \frac{\exp(-s)}{s} \tag{1}$$

between the Peclet number $P_{Iv}=\rho_{Iv}V/(2D)$ and the dimensionless undercooling $\Delta=(T_M-T_\infty)/(L/c_p)$ for a paraboloid of tip velocity V and tip radius ρ_{Iv} where D is the thermal diffusivity, T_M is the melting temperature, T_∞ is the initial temperature of the undercooled liquid, L is the latent heat of melting, and c_p is the specific heat at constant pressure.

In more recent history, the development of solvability theory [3,4] has led to the additional and crucial understanding that the anisotropic surface energy acts as a singular perturbation that uniquely selects the tip velocity, and also alters the entire dendrite shape [5–7]. According to this theory, the scaling parameter $\sigma^*=2Dd_0/\rho_{Iv}^2 V$ (where d_0, defined below, is the capillary length) approaches a constant at low undercooling that only depends on the anisotropy strength (denoted here by ϵ_4 for a crystal with an underlying cubic symmetry), and scales as $\sigma^* \sim \epsilon_4^{7/4}$ in the limit of vanishingly small anisotropy. In this same limit, Ben Amar and Brener [5] have predicted that capillary effects lead to a universal fourfold deviation from a paraboloid of the form

$$z=-\frac{r^2}{2}+A_4 r^4 \cos 4\phi, \tag{2}$$

where $A_4=1/88$ is independent of anisotropy strength and (r,ϕ) are the polar coordinates in the plane normal to the growth axis z with all lengths scaled by ρ_{Iv}. The improved prediction $A_4=1/96$ has been obtained in a subsequent analysis [6].

To characterize the shape further behind the tip, Brener remarked that the cross-sectional shape of needle crystal dendrites perpendicular to the growth axis can be assumed to evolve with increasing distance $|z|$ from the tip as a two-dimensional growth shape in time $(t=|z|/V)$. The area of this shape increases linearly in time, and thus $|z|$, as

$$S(z)=2\pi\rho_{Iv}|z|, \tag{3}$$

where ρ_{Iv} is defined by Eq. (1) with V being the actual tip velocity. This area corresponds to the well-known self-similarity solution of a growing circle in two dimensions and is also the exact cross-sectional area of the three-dimensional Ivantsov paraboloid of revolution. The above mapping is presumed to become justified far enough away from the tip where the component of the heat flux along z can be neglected. Using this mapping and the results of a previous analysis of two-dimensional anisotropic Laplacian growth at constant flux [8], he predicted that the width of the four dendrite fins should increase as the 3/5 power of the distance behind the tip [7], yielding the expression

$$z=-\frac{3}{5}\left(\frac{\sigma^*}{\sigma_2^*}\right)^{1/3}|x|^{5/3}, \tag{4}$$

where x is the interface coordinate normal to the z axis in a (010) section of the tip and σ_2^* (σ^*) is the tip scaling parameter in two (three) dimensions. Moreover, the ratio σ_2^*/σ^* becomes independent of anisotropy for weak anisotropy with $(\sigma_2^*/\sigma^*)^{1/3} \approx 1$.

Our goal in this paper is to use the phase-field method to obtain a characterization of the dendrite tip morphology that is sufficiently detailed and accurate to test the above theoretical predictions and to make a critical comparison with existing benchmark experiments [9,10]. The present simulations are based on a novel adaptive-step diffusion Monte

Carlo method [11,12] that provides an efficient treatment of the large scale diffusion field away from the growing structure. Thus this method allows us to investigate a relatively low undercooling range $\Delta \sim 0.1$ ($P_{Iv} \sim 0.03$), in contrast to previous simulations that were limited to Peclet numbers of order unity [13]. As it turns out, and this is one of the main findings in this paper, the tip morphology in this Peclet number range is already ostensibly independent of anisotropy strength and undercooling, except for a localized shape distortion at the tip that is not experimentally relevant. We are therefore able to compare meaningfully this morphology to existing detailed dendrite shape measurements in succinonitrile [9] and xenon [10], even though these measurements were carried out at even smaller Δ.

In the next section, we review the basic equations of the symmetric model of dendritic growth in three dimensions and briefly summarize our numerical methods. The numerical results are then presented in Sec. III and discussed in Sec. IV. Finally, a summary and conclusions are presented in Sec. V.

II. BASIC EQUATIONS

We study the standard symmetric model of solidification in a pure undercooled melt that assumes equal thermal diffusivities in the solid and liquid phases. The basic equations of this model are given by

$$\partial_t u = D\nabla^2 u, \tag{5}$$

$$v_n = D(\partial_n u|_s - \partial_n u|_l), \tag{6}$$

$$u = -d_0 \sum_{i=1}^{2} [a(\hat{n}) + \partial_{\theta_i}^2 a(\hat{n})]\kappa_i, \tag{7}$$

where following common notation, $u=(T-T_m)/(L/c_p)$ is the scaled temperature field that is zero in equilibrium and equal to $-\Delta$ in the liquid far from the interface, $\partial_n u|_l$ ($\partial_n u|_s$) is the normal gradient of u on the liquid (solid) side of the interface, v_n is the normal velocity of the interface, θ_i are the local angles between the normal $\hat{n}$ to the interface and the two local principal directions on the interface, κ_i are the principal curvatures, $d_0=\gamma_0 T_M c_p/L^2$ is the microscopic capillary length, and $\gamma(\hat{n})=\gamma_0 a(\hat{n})$ is the anisotropic surface energy where

$$a(\hat{n}) \equiv (1-3\epsilon_4)\left[1-\frac{4\epsilon_4}{1-3\epsilon_4}(n_x^4+n_y^4+n_z^4)\right] \tag{8}$$

for a material with an underlying cubic symmetry, with the x, y, and z axes chosen parallel to the [100] directions. In writing down the interface condition (7), we have purposely neglected the effect of interface kinetics that is believed to be negligible for the low undercooling range where benchmark shape measurements have been carried out [9,10]. Moreover, theoretical shape predictions to date [5–7] have neglected this effect.

We use two different numerical methods. The first, and main one used here, is the phase-field approach [14,15] that allows us to study the dendrite shape for the full cubic form of the surface energy defined by Eq. (8). In particular, we simulate the time-dependent evolution of a single dendrite arm until steady-state growth is reached. Since we are primarily interested in a low undercooling regime, we use the results of the asymptotic analysis of Karma and Rappel [13] in order to choose the interface width in the phase-field model about an order of magnitude smaller than ρ, and thus much larger than d_0 for small Δ. This analysis also allows us to choose the model parameters so as to make kinetic effects vanishingly small. Moreover, we use a recently developed Monte Carlo algorithm to integrate efficiently the diffusion equation in the liquid away from the growing structure. In this approach, space is divided into two regions. The first region consists of the solid plus a thin liquid layer surrounding the interface where the deterministic phase-field equations are solved on a cubic lattice with the same choice of computational parameters as in Ref. [13]. The second region is the rest of the liquid where the diffusion equation is solved using an ensemble of random walkers that take progressively larger steps with increasing distance away from the interface. The algorithm used to interface the deterministic and stochastic solutions of the diffusion equation in these two regions and to update the walkers has been summarized in Ref. [11] where it was used to study the early stage of dendritic evolution. It has also been exposed in more details in Ref. [12] together with the results of numerical tests and need not be redescribed here.

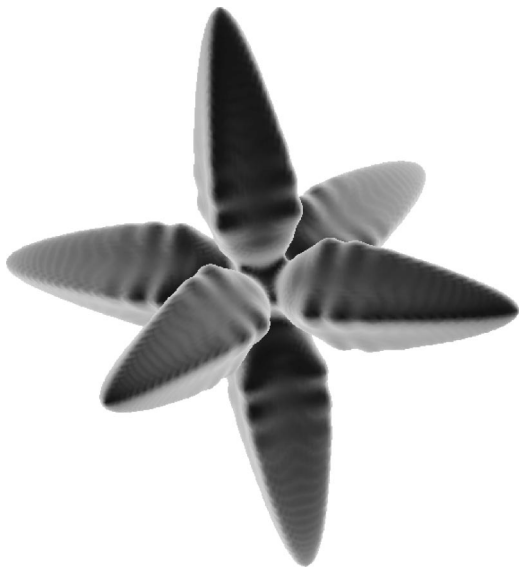

FIG. 1. Snapshot of a three-dimensional simulated dendrite with $\Delta=0.1$ and $\epsilon_4=0.025$.

We exploit the cubic symmetry to reduce simulation time by only integrating a part of a single dendrite arm (the domain $x>0$, $0<y<x$ and $z>x$), taking advantage of the symmetry planes defined by $x=0$, $y=0$, $x=y$, and $x=z$. The whole dendrite can then be reconstructed by successive reflections at these planes, and the result of one of our simulations is shown in Fig. 1. These simulations were performed on regular lattices of size $240\times240\times800$ and each took about 200 h of CPU time on a 525 MHz DEC-8400 computer. Note that almost no sidebranches can be discerned, although the length of the dendrite arms is more than 40 times the tip radius of curvature. For the analysis of the steady-state shapes, we used only the part of the dendrite

grown at a constant tip velocity, which corresponds to about one third of the arm length in Fig. 1. To check whether the shape is well converged, we performed one run in which the dendrite arm growing along the positive z direction was ''cut off'' sufficiently far behind the tip, and its further evolution was simulated in a smaller box moving with the dendrite tip for several diffusion times (D/V^2). No significant change of the shape was observed. In addition, this run (for $\Delta=0.1$ and $\epsilon_4=0.025$) yielded data which extend considerably farther behind the tip than for the other parameters, well to within the range where sidebranches are observed in experiments.

The second numerical method is the standard boundary integral method [16] that can be used to solve directly the sharp-interface steady-state growth equations with the simplified axisymmetric form of surface energy

$$a(\hat{n}) \equiv (1-3\epsilon_4)\left[1-\frac{4\epsilon_4}{1-3\epsilon_4}\left(\cos^4\theta+\frac{3}{4}\sin^4\theta\right)\right], \quad (9)$$

which is obtained by averaging the full cubic form (8) over the polar angle ϕ in the x-y plane; θ is the angle between the local normal to the solid-liquid interface and the z axis. This method only describes axisymmetric tip shapes and is thus only used here as an additional basis of comparison with phase-field results regarding the anisotropy-dependent shape distortion in the tip neighborhood and the selected tip operating state.

III. NUMERICAL RESULTS

A. Equal cross-sectional area shape

The cross-sectional area of solid normal to the growth axis was calculated using the formula

$$S(z)=\int \frac{1}{2}[\psi(x,y,z)+1]\,dx\,dy, \quad (10)$$

where $\psi(x,y,z)$ is the phase field that varies from $+1$ in the solid to -1 in the liquid in the present model [13] and $\psi(x,y,z)=0$ defines the solid-liquid interface. This formula is accurate far enough away from the tip, but of course not at the tip itself, which suffices for the present purposes. Plots of $S(z)$ vs $|z|$ are shown in Fig. 2 for different undercoolings and anisotropy strengths. $S(z)$ is accurately fitted by a straight line sufficiently away from the tip. This allows us to define the ''parabolic'' tip radius, ρ_p, of a paraboloid of revolution with the same cross-sectional area as the nonaxisymmetric phase-field shape. Such a paraboloid has a cross-sectional area

$$S_p(z)=2\pi\rho_p(z_0-z) \quad \text{for} \quad z<z_0, \quad (11)$$

where z_0 is its tip position. By fitting the linear part of $S(z)$ away from the tip computed from Eq. (10) with Eq. (11), we obtain an accurate estimate of ρ_p (note that z_0 need not coincide with the tip position of the full nonaxisymmetric shape, see below). The quality of this fit will be illustrated below in Fig. 17, where it is compared to a different method for determining ρ_p.

Remarkably, and in good agreement with theoretical expectation [Eq. (3)], ρ_p coincides to within a numerical accuracy of 1–2 % with the Ivantsov tip radius $\rho_{Iv}\equiv 2DP_{Iv}/V$ of the isothermal paraboloid growing with the same tip velocity as the phase-field shape for the different undercoolings and anisotropies investigated here. This indicates that $\rho_p \approx \rho_{Iv}$ is potentially a good scaling parameter for the entire dendrite shape, as will be confirmed below. Therefore, unless otherwise stated, all lengths will be rescaled by ρ_{Iv} for the reminder of this paper. The origin of the z axis is chosen to coincide with the tip position of the nonaxisymmetric dendrite shape.

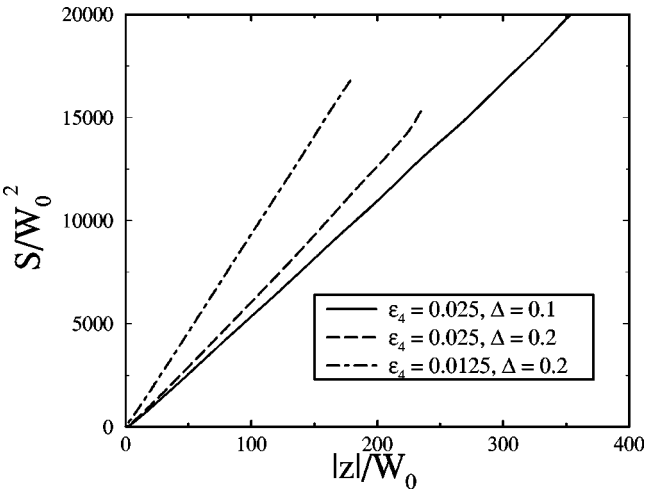

FIG. 2. Plot of the cross-sectional area $S(z)$ vs distance $|z|$ from the tip for different growth parameters. Lengths are measured here in units of W_0, the thickness of the diffuse interfaces in the phase-field model as defined in Ref. [13].

It is also useful to define the equal cross-sectional area (ECSA) shape

$$r_0(z)=\left[\frac{1}{2\pi}\int_0^{2\pi} d\phi\, r^2(z,\phi)\right]^{1/2}=\left[\frac{S(z)}{\pi}\right]^{1/2}, \quad (12)$$

where $r(z,\phi)$ is the radial coordinate of the full nonaxisymmetric shape. This is simply the axisymmetric shape that has the same cross-sectional area as the full shape, and the above results imply at once that $r_0(z)$ coincides away from the tip with the Ivantsov paraboloid. The ECSA shape is shown as solid squares in Fig. 3 together with the parabolic fit obtained by using Eqs. (11) and (12). The parabolic fit is extended all the way to its tip position z_0 for illustrative purposes.

B. Nonaxisymmetric tip morphology

Longitudinal sections of the dendrite tip in the $\phi=0°$ and $\phi=45°$ planes that correspond to the ''fins'' and ''valleys'' of the nonaxisymmetric shape, respectively, are superimposed in Fig. 3. The two contours coincide in the upper region of the tip, where the shape is essentially axisymmetric, but depart from a paraboloid (dashed line in Fig. 3) in a small region near the tip that will be examined more closely in Sec. III C. The important point here, especially relevant for comparisons between simulations and experiments, is that aside from this localized tip distortion the entire tip shape scales with ρ_{Iv} and is ostensibly independent of anisotropy strength and undercooling over the range investigated here. This is clearly demonstrated by the nearly perfect superposition of longitudinal and transverse sections of the

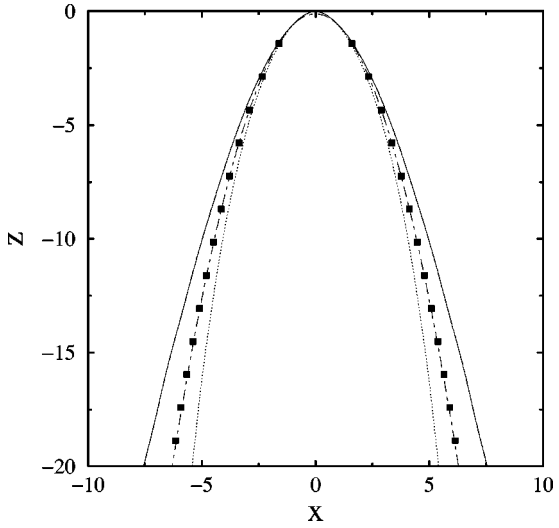

FIG. 3. Sections of phase-field shapes in the $\phi=0°$ plane (solid line) and $\phi=45°$ plane (dotted line), equal cross-sectional area shape (solid squares), and parabolic fit of the latter (dashed line). Parameters are $\Delta=0.1$ and $\epsilon_4=0.025$.

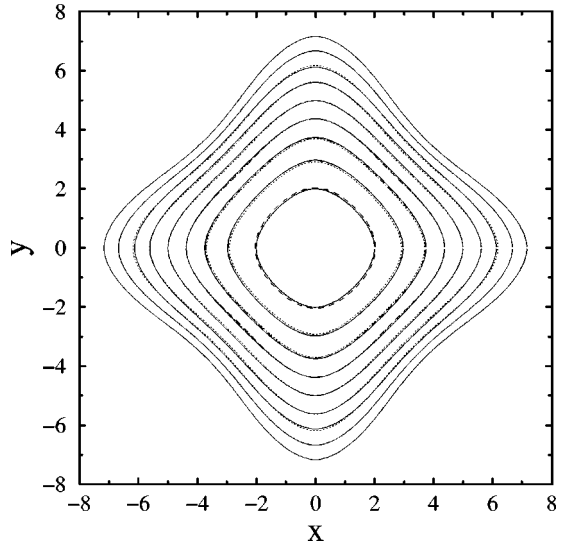

FIG. 5. Superposition of transverse tip sections for $\epsilon_4=0.025$, $\Delta=0.1$ (solid lines), $\epsilon_4=0.025$, $\Delta=0.2$ (dotted lines), and $\epsilon_4=0.0125$, $\Delta=0.2$ (dashed lines). Cross sections are taken at $|z|/\rho_{Iv}=2,4,6,\ldots$.

various tip shapes shown in Figs. 4 and 5, respectively. A three-dimensional view of this universal tip morphology is shown in Fig. 6.

In order to test if the analytical form defined by Eq. (2) provides an accurate description of the nonaxisymmetric tip shape, we determined A_4 by minimizing the spatially averaged root-mean-square (rms) deviation $\langle \delta z^2 \rangle^{1/2}$, between the actual shape in the (010) plane and the polynomial form $z=-r^2/2+A_4 r^4$ over the interval $1 \leqslant |z| \leqslant n$ where n was varied from 4 to 20 in steps of 2. The resulting values of A_4 and $\langle \delta z^2 \rangle^{1/2}$ are plotted for the different undercoolings and anisotropy strengths in Figs. 7 and 8, respectively. Figure 8 shows that the form (2) provides a good fit of the fin shape for n up to about 10, after which the rms deviation starts to increase rather sharply. Figure 7, in turn, shows that the fitted value of A_4 depends on the fitting length. This means that the polynomial form (2) does not exactly characterize the fin shape. However, the dependence of A_4 on n is rather weak: A_4 varies between about 0.004 and 0.005 for n between 4 and 10. A comparison of the polynomial fit and the computed fin shape is shown in Fig. 9, showing an excellent overlap up to $10\rho_{Iv}$ behind the tip.

We have examined how the form (2) with the above procedure to determine A_4 fits the entire nonaxisymmetric shape, and not just the fin. This is illustrated in Fig. 10 where we compare the transverse sections of the computed phase-field tip shape with the ones corresponding to the form (2).

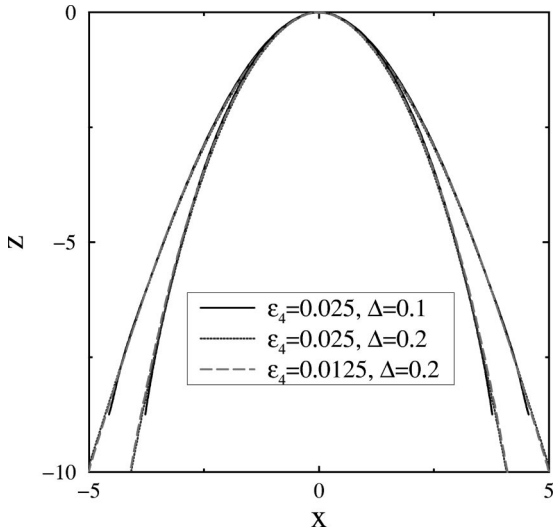

FIG. 4. Superposition of dendrite contours taken along fins and valleys for different parameters.

FIG. 6. Three-dimensional view of the simulated tip morphology for $\Delta=0.1$ and $\epsilon_4=0.025$.

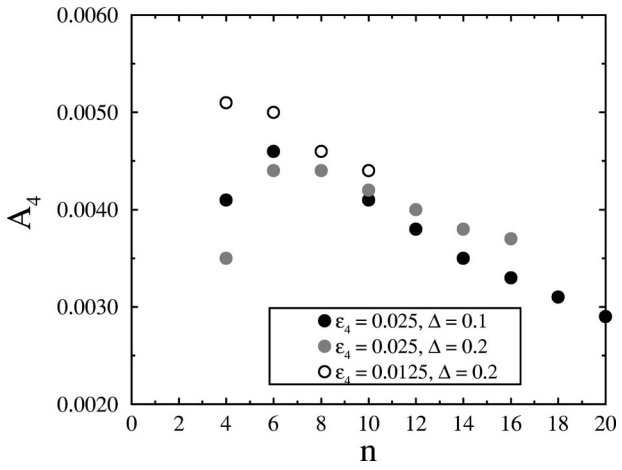

FIG. 7. Plot of A_4 vs n obtained from a fourth order polynomial fit of the fin shape over the interval $\rho_{Iv} \leq |z| \leq n\rho_{Iv}$.

The two are in good agreement up to ten ρ_{Iv} behind the tip, although a small deviation due to higher azimuthal harmonics is noticeable.

We have also fitted the fin shape to the power law $z = -a|x|^{\beta}$ by minimizing the rms deviation from the computed shape as above. This minimization was carried out both with a and β as free parameters and with a as free parameter and β fixed to the theoretically expected value 5/3. The values of a and β resulting from these two fits are plotted vs the fitting range parameter n in Fig. 11 with the corresponding rms deviations plotted in Fig. 8. In the two-parameter fit, β is larger than 5/3 (≈ 1.8) for small n and tends to 1.7 for larger n, which is close to 5/3. Note that the value of a is somewhat smaller in the two-parameter fit than in the one parameter fit because of the larger β in the former, and that the two-parameter fit has a smaller rms deviation as one would expect. The two fits, however, become essentially equally good for large n. In this range, the one-parameter fit yields $a \approx 0.68$ independent of anisotropy strength. A comparison of the power law fit and the computed fin shape is shown in Fig. 9. In contrast to the polynomial fit, which becomes inaccurate for $|z| > 10\,\rho_{Iv}$, the power law closely fits the fin shape even far away from the tip.

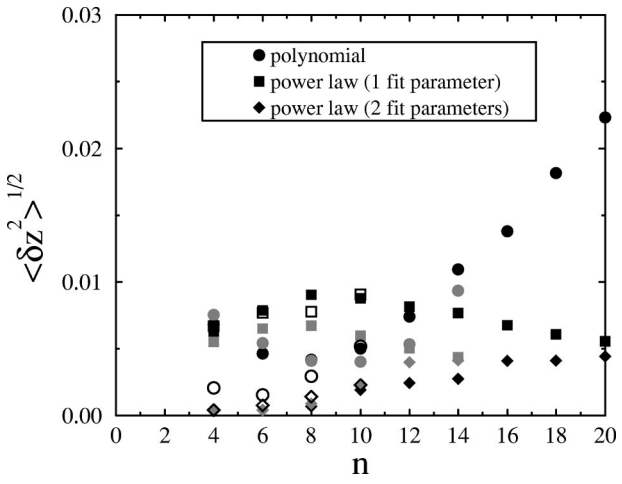

FIG. 8. Plot of the root-mean-square shape deviation corresponding to the polynomial and power law fits versus the fitting length. Black symbols: $\epsilon_4 = 0.025$, $\Delta = 0.1$; grey symbols: $\epsilon_4 = 0.025$, $\Delta = 0.2$; open symbols: $\epsilon_4 = 0.0125$, $\Delta = 0.2$.

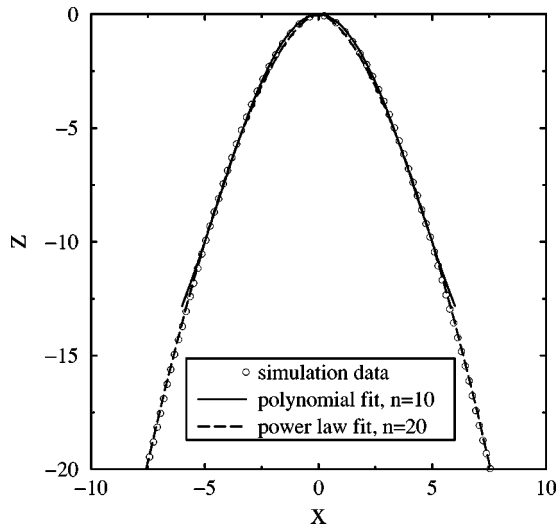

FIG. 9. Comparison of the computed fin shape (open circles) with the polynomial fit for $n = 10$ ($A_4 = 0.004$, solid line) and the power law fit for $n = 20$ and $\beta = 5/3$ ($a = 0.685$, dashed line).

C. Localized tip distortion and tip radius

Let us now return to examine more closely the shape departure from a paraboloid in the region very close to the tip. For this purpose, we show in Fig. 12 a tip magnification of the same curves as in Fig. 3, together with the axisymmetric shape computed by the boundary integral method for an azimuthally averaged surface energy. The latter coincides well with the fins and valleys in the tip neighborhood, but the superposition of these three curves departs from the parabolic fit of the ECSA shape, which represents the interface shape if anisotropic capillary effects were absent. Note also that the boundary integral result starts to deviate noticeably from the phase-field shape rather close to the tip, approximately at $|z| \approx 0.5\,\rho_{Iv}$.

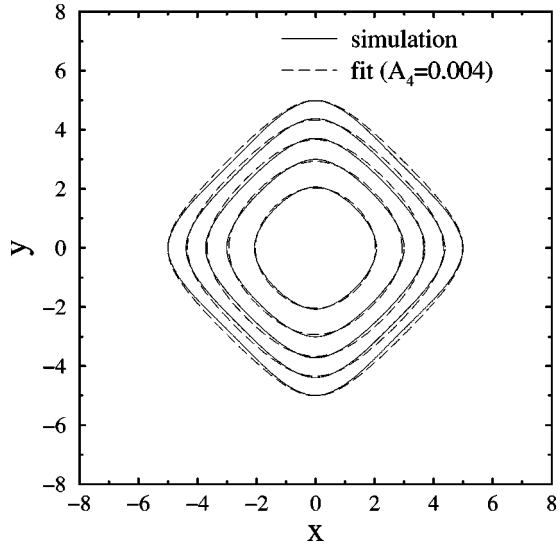

FIG. 10. Comparison of the computed tip cross-sections for $\epsilon_4 = 0.025$, $\Delta = 0.1$, and the shape given by Eq. (2) with $A_4 = 0.004$. Cross sections are taken at $|z|/\rho_{Iv} = 2, 4, 6, 8,$ and 10.

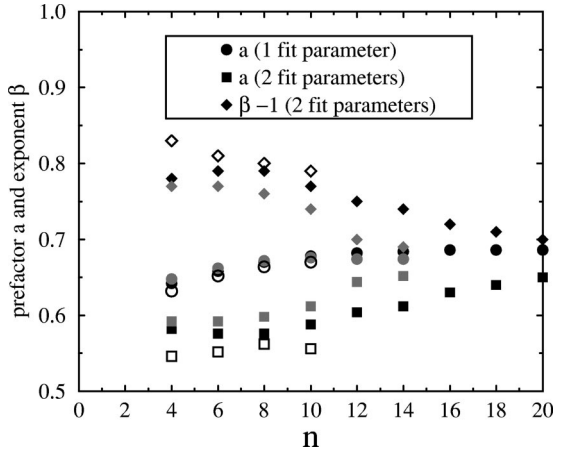

FIG. 11. Plot of the prefactor a and exponent β vs the fitting range parameter n. Black symbols: $\epsilon_4=0.025$, $\Delta=0.1$; grey symbols: $\epsilon_4=0.025$, $\Delta=0.2$; open symbols: $\epsilon_4=0.0125$, $\Delta=0.2$.

A quantitative measure of this departure is the ratio ρ/ρ_{Iv}, where ρ is the actual numerically computed tip radius of the phase-field or boundary integral shape and ρ_{Iv} [recall that $\rho_{Iv}\equiv 2DP_{Iv}/V$ where P_{Iv} is the Peclet number predicted by Eq. (1) and V is the numerically computed tip velocity]. For the phase-field shape, ρ is computed from the $\phi=0°$ section using the interpolation scheme that is described in Appendix B of Ref. [13], and which has been tested against exact boundary integral benchmark results in two dimensions.

Figures 13 and 14 show the variation ρ/ρ_{Iv} as a function of undercooling and anisotropy, respectively. The departure of ρ from the Ivantsov relation increases with anisotropy strength. The same trend was previously found for a higher undercooling ($\Delta=0.45$) in Ref. [13] and the results of these earlier simulations are also shown in Fig. 14. A new finding here is that this departure becomes independent of undercooling in the low undercooling range studied here as can be seen from the flattening of the curves at small Δ in Fig. 13. For $\Delta\sim 0.1$, ρ/ρ_{Iv} is already quasi-independent of Δ and its small Δ limiting value depends solely on the anisotropy strength. Interestingly, the variation of ρ/ρ_{Iv} with anisotropy is crudely approximated by the relation

$$\rho/\rho_{Iv}\approx 1-\alpha, \tag{13}$$

over an order of magnitude change in anisotropy strength, where $\alpha=15\epsilon_4$ is the stiffness anisotropy. Since the Gibbs-Thomson condition (7) implies that the steady-state dendrite tip temperature is given by

$$u_{tip}=-2d_0(1-\alpha)/\rho, \tag{14}$$

Eq. (13) is equivalent to stating that the dendrite tip temperature at a given undercooling is relatively independent of anisotropy strength. The straight line corresponding to Eq. (13) is superimposed as a dashed line in Fig. 14. The numerical results lie slightly above and below this curve for small and large anisotropy, respectively.

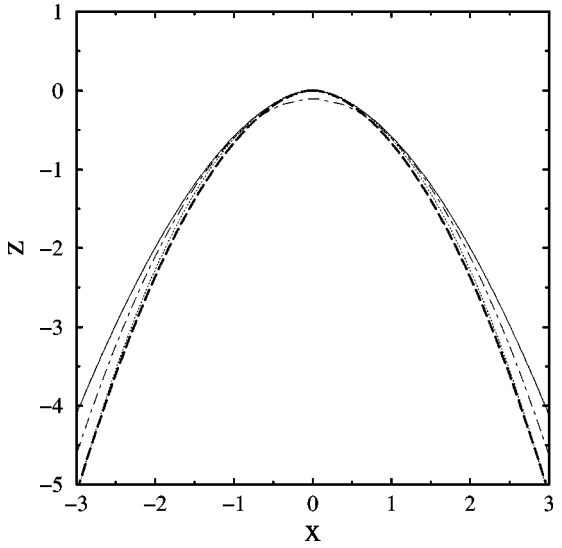

FIG. 12. Magnification of the tip region showing the same curves as in Fig. 3, with the solid squares omitted for clarity. Also superimposed is the axisymmetric shape computed by the boundary integral method for an azimuthally averaged surface energy (thick dashed line). Parameters are $\Delta=0.1$ and $\epsilon_4=0.025$.

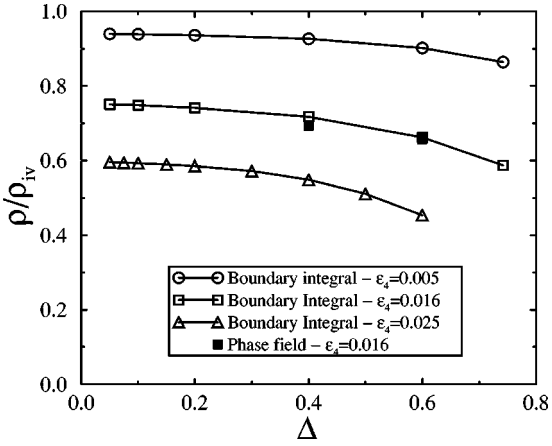

FIG. 13. Ratio ρ/ρ_{Iv} versus dimensionless undercooling Δ for different anisotropies. Lines are drawn as a guide to the eye.

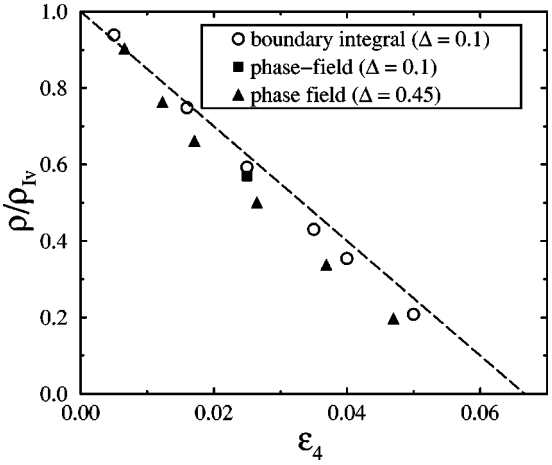

FIG. 14. Ratio ρ/ρ_{Iv} versus anisotropy for $\Delta=0.1$, and for $\Delta=0.45$ from Ref. [13]. Superimposed is the constant tip temperature relation $\rho/\rho_{Iv}=1-15\epsilon_4$ (dashed line).

IV. DISCUSSION

A. Comparison with analytical theories

Let us first compare our results with the analytical theories reviewed in the introduction. We have found that Eq. (2) provides a good fit of the tip shape up to a distance of about eight to ten ρ_{Iv} behind the tip. Moreover, for low undercooling, this shape is independent of anisotropy strength (at least over the range investigated here) which is in qualitative agreement with the prediction of linear solvability theory [5,6]. The value of A_4 found here, however, is about twice smaller than the value $A_4=1/96\approx 0.104$ [6] predicted by this theory. One possible reason for this discrepancy is that the existing solvability calculations [5,6] are carried out in the limit of vanishing anisotropy, whereas in the present computations the anisotropy is finite. We have seen, however, that even for a short fitting distance behind the tip, A_4 increases from about 0.004 to 0.005 when the anisotropy is lowered from 2.5 to 1.25 %, which does not appear consistent with an extrapolation of A_4 to its theoretically predicted value in the limit that $\epsilon_4\rightarrow 0$. It seems also difficult to explain this discrepancy by the fact that existing calculations are based on linearizing the steady-state growth equations around a paraboloid of revolution. We find indeed a localized tip distortion that depends strongly on anisotropy strength, and which is not accounted for in these theories. The rest of the tip shape, however, departs only weakly from a paraboloid and is well fitted by the form (2) independently of anisotropy. Therefore, the origin of this discrepancy remains to be understood.

In contrast, the predicted power law [Eq. (4)] for the fin shape away from the tip is in relatively good quantitative agreement with the present simulations. We find a good fit of the fin shape with a fixed exponent $\beta=5/3$ and a prefactor $a\approx 0.68$ that is independent of anisotropy strength and only about 15% larger than theoretically predicted, or with a slightly higher exponent $\beta=1.7$ and a lower $a\approx 0.65$. It is interesting to note that the mapping with two-dimensional growth shapes [7] implies that Eq. (4) should only strictly hold in a region far behind the tip where the cross-sectional shape contains four well-developed arms. It is therefore rather remarkable, and perhaps coincidental, that it also holds closer to the tip in a region where the fins are not yet well developed. Finally, we note that our results indicate a smooth crossover from a polynomial form to a power law form for the fin shape with increasing $|z|$. This is indicated by the excellent overlap of these two forms in an intermediate distance range behind the tip (Fig. 9).

B. Comparison with experiments

On the experimental side, the most detailed shape measurements to date have been carried out by LaCombe *et al.* who analyzed the full three-dimensional tip morphology in succinonitrile (SCN) [9] and by Bisang and Bilgram who studied the fin shape in xenon [10]. On the basis of their measurements on SCN dendrites, Lacombe *et al.* reported that the tip shape can be fitted by the form

$$z\approx -\frac{r^2}{2}-Q(\phi)\,r^4, \tag{15}$$

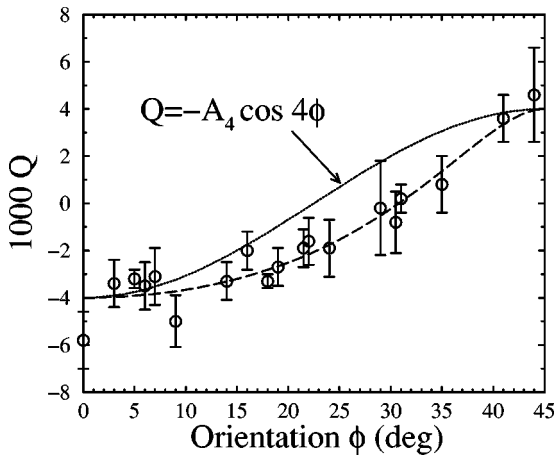

FIG. 15. Function $Q(\phi)$ from the experimental measurements of LaCombe *et al.* in SCN [9] (circles and error bars; some points close to $\phi=0°$ have been omitted). The function $Q(\phi)$ computed here from the projections of the shape defined by Eq. (2) with $A_4=0.004$ is shown as a dashed line. This curve differs from a pure cosine function, which is also shown for comparison.

where lengths are in units of the tip radius. The values for the function $Q(\phi)$ reported by these authors and the associated error bars are reproduced here in Fig. 15. It can be seen that $Q(\phi)$ differs from a cosine function, and they concluded that the tip morphology cannot be described by a pure $\cos 4\phi$ mode, in apparent disagreement with solvability theory and the present results. This function, however, was constructed from *projected shapes* obtained by taking photographs of the dendrite tip from different azimuthal angles ϕ. We point out here that Eq. (15) with $Q(\phi)$ obtained from projected shapes does not correctly represent the actual nonaxisymmetric tip morphology from which these projections are obtained. The reason is that the projected shape observed from a given azimuthal angle ϕ differs from the cross-sectional shape at this angle. To illustrate this point, we have drawn in Fig. 16 a cross section of the tip shape normal to the growth direction and rotated it by an angle ϕ with respect to the viewing direction chosen parallel to the Y axis. The projected shape appears wider than the ''true'' contour of the dendrite at that orientation. Therefore, the dendrite cross sections (Fig. 11 in Ref. [9]) reconstructed by LaCombe *et al.* using Eq. (15) are not representative of the true cross sections.

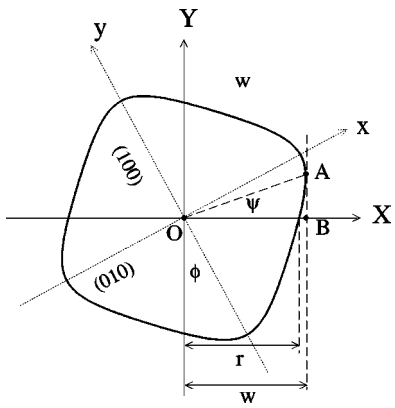

FIG. 16. Sketch illustrating the difference between the contour of a dendrite as seen under an angle ϕ with respect to a (010) plane and the ''true'' dendrite contour at this angle.

It is nonetheless possible to relate our results to the experimental measurements of these authors by calculating numerically the function $Q(\phi)$ that corresponds to the tip morphology characterized by a single $\cos 4\phi$ mode [Eq. (2)]. As mentioned earlier, Eq. (2) with $A_4=0.004$ provides a good fit to our simulated tip morphology up to $10\rho_{Iv}$ behind the tip and is therefore adequate for the purpose of this comparison (neglecting small corrections due to higher azimuthal harmonics). To obtain $Q(\phi)$, we must first calculate numerically the projected shape, and thus relate the *apparent* width $w(\phi,z)$ of the dendrite at a given distance z behind the tip to the true width $r(-\phi,z)$, which is the intersection of the fixed X axis with the interface. Using the definitions of Fig. 16 and purely geometrical considerations, it is simple to obtain the relation

$$w(\phi,z)=r(\psi-\phi,z)\cos\psi, \tag{16}$$

where $\psi(\phi,z)$ is defined implicitly by the relation

$$\psi=\arctan\left[\frac{\partial_\psi r(\psi-\phi,z)}{r(\psi-\phi,z)}\right]. \tag{17}$$

Equation (17) follows directly from the condition that the point on the true contour that corresponds to the apparent (perceived) edge of the solid tip (point A in Fig. 16) be the one of maximum width as a function of ψ. For a fixed ϕ, the corresponding ψ can be simply obtained by setting equal to zero the derivative of the right-hand side of Eq. (16) with respect to ψ. The angle ψ defined implicitly by Eq. (17) is then the polar coordinate of this point measured from the fixed X axis in Fig. 16, and $\phi-\psi$ measures the angle between the line OA and the (010) plane. Note that at this point, Eqs. (16) and (17) can be used to construct the projected shape that corresponds to an arbitrary true shape whose transverse sections are convex. To proceed further, we now restrict our attention to the case where the true shape is given by Eq. (2), or equivalently

$$r(\phi,z)=\left[\frac{1-\sqrt{1-16zA_4\cos 4\phi}}{4A_4\cos 4\phi}\right]^{1/2}. \tag{18}$$

Combining Eqs. (16)–(18), we obtain numerically the projected shape $z(\phi,w)$ that is the inverse of $w(\phi,z)$ at fixed ϕ. We finally obtain $Q(\phi)$ by following the same procedure as LaCombe *et al.* that consists of fitting these shapes to a fourth order polynomial of the form

$$z\approx -w^2/2-Q(\phi)w^4 \tag{19}$$

for different values of ϕ. This procedure yields a function $Q(\phi)$ that differs from $\cos 4\phi$ and is superimposed as a dashed line in Fig. 15. This function fits well through the data points for $Q(\phi)$ reported by LaCombe *et al.* We therefore conclude that, within experimental error bars, our simulated universal tip morphology dominated by a single $\cos 4\phi$ mode with an amplitude $A_4\approx 0.004$ agrees quantitatively well with the true underlying tip morphology of SCN dendrites.

A few additional remarks should be made. First, in drawing the above conclusion we have implicitly assumed that the inverse problem that consists of reconstructing the true shape from its projections has a unique solution. It can indeed be shown that this solution is unique [17], such that this assumption is valid. That is if we were to calculate the true shape from the projections defined by Eq. (19), we would recover a tip shape that is well fitted by Eq. (2). Moreover, an explicit solution to this inverse problem can be obtained analytically by cleverly noting [17] that it is exactly analogous to the one of constructing a two-dimensional equilibrium crystal shape, with the role of the anisotropic surface energy being played here by $w(\phi,z)$ at fixed z. This is the well-known Wulff construction [18] and the application of the ξ-vector formalism of Cahn and Hoffman [19] yields that the distance AB in Fig. 16 is equal to $|\partial_\phi w(\phi,z)|$, and thus that the solution to this inverse problem is given by

$$r(\psi-\phi,z)=\sqrt{[w(\phi,z)]^2+[\partial_\phi w(\phi,z)]^2}, \tag{20}$$

$$\psi=-\arctan\left[\frac{\partial_\phi w(\phi,z)}{w(\phi,z)}\right]. \tag{21}$$

In principle, it should therefore be possible to reconstruct the higher azimuthal harmonics from the experimental data. At present, however, such an analysis is precluded by the magnitude of the error bars in the measurements, especially in view of the small amplitude of such harmonics predicted by our simulations. Lastly, we note that in the present example the exact (numerically computed) projected shapes $z(\phi,w)$ defined by Eqs. (16)–(18) are only approximately fitted by fourth order polynomials in w, even though the underlying true shapes defined by Eq. (2) are exact fourth order polynomials in r. It is simple to see why this is so by using Eqs. (16)–(18) to derive an analytical expression for the projected shape in powers of A_4 (valid close to the tip), and by noting that this expansion generates terms $\sim w^6$ at $O(A_4^2)$. Nonetheless, the form [Eq. (19)] provides a reasonably accurate global fit of the projected shape over the range $0<|z|<10$ and is therefore quantitatively adequate to interpret experimental results.

In xenon, Bisang and Bilgram have reported that they cannot accurately fit the fin shape with a low order polynomial. They find, instead, a good fit with a power law $|z|=ax^\beta$ with $a=0.58\pm 0.04$ and $\beta=1.67\pm 0.05$, that extends rather close to the tip. Our present results differ from theirs in that both for the polynomial and the power law fit, the fitting parameters vary with the fitting length, including the exponent β which increases when the fit is restricted to a region close to the tip. On the other hand, in agreement with their findings, the polynomial fit becomes inaccurate for larger fitting lengths, whereas the power law fits the fin shape even far behind the tip. While the exponents obtained from our simulations and their measurements are very close, we find here a slightly larger prefactor $a\approx 0.68$, independently of anisotropy. Note, however, that this discrepancy might be simply due to the choice of the rescaling length. Bilgram and Bisang use the actual tip radius as a scaling length, whereas we use the Ivantsov tip radius. Taking this into account, their prefactor a' and our prefactor a should be related by $a'=a(\rho/\rho_{Iv})^{\beta-1}$. As ρ is smaller than ρ_{Iv}, our prefactor should indeed be larger than theirs. It would be interesting to reexamine the experimental data using ρ_{Iv} as the scaling length.

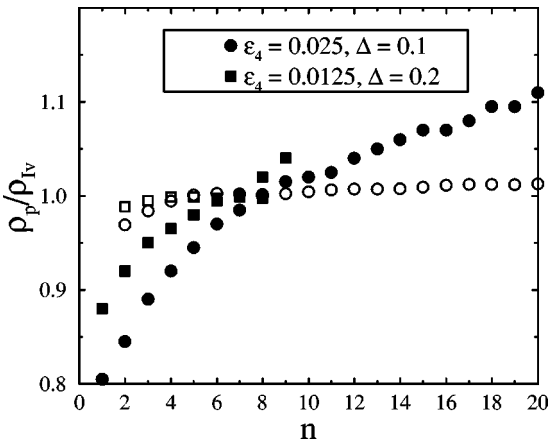

FIG. 17. Plot of the parabolic tip radius ρ_p versus the fitting range n ($|z|<n\rho_{Iv}$) in a fit using Eq. (26) with both ρ_p and A_4 as fit parameters. For comparison, the results obtained from a fit of the equal cross-sectional area shape according to Eq. (11) are shown as open symbols.

C. Tip distortion

The tip distortion analyzed in Sec. III C can be interpreted to result from capillary effects at the tip that persist even in the limit of low undercooling. It may appear at first counterintuitive that such effects remain important in this limit since the magnitude of capillary corrections to the tip temperature vanishes due to the increase of the tip radius, i.e., $d_0/\rho \to 0$ as $\Delta \to 0$. One must recall, however, that the tip velocity and thus the temperature gradient at the tip also vanishes in this limit. Thus the correct measure of the relative importance of capillary effects is the ratio of the magnitudes of the normal gradient of u in the tip region induced by capillary variations, $(\partial_n u)_c \sim d_0/\rho^2$, and by heat diffusion, $(\partial_n u)_d \sim V/D$, or $(\partial_n u)_c/(\partial_n u)_d \sim Dd_0/(\rho^2 V) \sim \sigma^*$. The constancy of σ^* implies that capillary effects can produce a non-negligible tip distortion that persists in the low undercooling limit.

With regard to the tip radius, Eq. (13) can be crudely interpreted to be the simplest linear interpolation between the isotropic limit where the tip radius approaches its isothermal value, and the limit $\alpha \to 1$ ($\epsilon_4 \to 1/15$) which marks the appearance of cusps at the [100] orientations of the equilibrium shape where ρ vanishes. There is, of course, no obvious reason why this linear interpolation should exactly hold in between these two limits and Fig. 14 shows that our numerical results do not lie exactly on it. Equation (13) should only be considered a reasonable first estimate of the actual tip radius.

D. Operating state

Traditionally, the operating state of the dendrite tip has been characterized in terms of two independently measurable parameters, the tip radius ρ and velocity V, from which one defines the scaling parameters

$$P = \frac{\rho V}{2D}, \tag{22}$$

$$\sigma^* = \frac{2Dd_0}{\rho^2 V}. \tag{23}$$

It is clear, however, from the present results that an accurate measurement of the ''true'' tip radius is most likely not experimentally feasible. Such a measurement would require a very high resolution of the localized shape distortion near the tip that is already barely noticeable on the scale of Fig. 3 for a 2.5% anisotropy, and with the interface and the reference parabola represented by thin lines that are finer than the experimental resolution.

The present results show that, outside the small region very close to the tip where this distortion is noticeable, the entire tip shape is well fitted by a paraboloid with a small nonaxisymmetric fourfold deviation, and that the rest of the dendrite shape further away from the tip scales with the tip radius ρ_p of this paraboloid. Therefore, a better definition of the tip operating state is to use ρ_p instead of ρ and to define accordingly the dimensionless parameters

$$P_p = \frac{\rho_p V}{2D}, \tag{24}$$

$$\sigma_p^* = \frac{2Dd_0}{\rho_p^2 V}, \tag{25}$$

which are actually the ones that have been traditionally measured in experiments. In addition, the definition of σ^* used in solvability theories (see Sec. I) coincides with the latter definition with the further assumption that $\rho_p = \rho_{Iv}$. For a weakly anisotropic material such as SCN ρ is not too different from ρ_p such that the two definition sets [Eqs. (22),(23) and (24),(25)] are roughly equivalent. In contrast, for a more strongly anisotropic material such as pivalic acid (PVA), ρ_p can be about two to five times larger than ρ, and concomitantly σ_p^* four to twenty-five times smaller than σ^* if we assume that ϵ_4 is somewhere in the range $0.025-0.05$, where the lower limit has been measured by Muschol *et al.* [20] and the upper one by Glicksman and Singh [21].

If we adopt Eqs. (22),(23) as a definition of the tip operating state, three questions remain to be addressed. First, what is the best way to measure ρ_p? Second, how accurately does linear solvability predict the tip operating state as compared to the present simulations? Lastly, does ρ_p necessarily equal ρ_{Iv}, as found here and assumed in solvability theory?

In our simulations, we have obtained ρ_p in Sec. III A from a plot of the cross-sectional area of the dendrite versus distance from the tip, exploiting the fact that, away from the tip, ρ_p is simply the slope of this curve divided by 2π. This provides a very accurate procedure, as can be demonstrated by plotting the resulting value for ρ_p versus the fitting range (Fig. 17): for n between 4 and 10, ρ_p varies by less than one percent. The dendrite cross section, however, is not easy to measure as the true dendrite shape is difficult to reconstruct from longitudinal projections for the reasons emphasized in Sec. IV B. The best data are obtained for the fin shape [9,10]. One way to extract ρ_p is therefore to fit the unrescaled fin shape with a fourth order polynomial

$$z = -(r/\rho_p)^2/2 + A_4(r/\rho_p)^4, \tag{26}$$

TABLE I. Comparison of the selection constants σ^* obtained from the present phase-field simulations, from linear solvability theory, and from boundary integral calculations.

	Δ	ϵ_4	$\sigma^\star$	$\sigma_p^\star$
Phase-field	0.2	0.025	0.171	0.0565
Linear solvability				0.067
Boundary integral			0.150	0.055
Phase-field	0.1	0.025	0.181	0.0611
Linear solvability				0.069
Boundary integral			0.155	0.059
Phase-field	0.2	0.0125	0.0447	0.0282
Linear solvability				0.0294
Boundary integral			0.0394	0.0265

over a varying distance from the tip where both ρ_p and A_4 are allowed to vary, which is the method used by LaCombe *et al.* in SCN [9]. We have carried out this same procedure on our computed fin shapes and the results are shown in Fig. 17 for two different anisotropies. [Note that this fit differs from the one carried out in Sec. III B where we fixed ρ_p to its value ($\approx\rho_{Iv}$) extracted from the cross-section measurement, and only varied A_4.] One can see that ρ_p increases with the fitting distance ($=n\rho_{Iv}$) behind the tip, which renders a precise determination of ρ_p difficult. This trend was observed by Bisang and Bilgram in xenon dendrites [10]; on the other hand, for SCN, where ϵ_4 is about twice smaller than the lowest anisotropy studied here, LaCombe *et al.* find that ρ_p is almost constant when n varies between 4 and 10. It is therefore possible that this fitting procedure improves for lower anisotropies. Figure 17 also shows that the departure of the fitted radius from ρ_{Iv} is of the order of a few percent for fitting ranges around $n=10$, such that this method can provide a reasonable estimate.

We compare in Table I the values of σ_p^* predicted by the linear solvability theory of Barbieri and Langer [23] with the values corresponding to the nonaxisymmetric shapes of the phase-field model and the axisymmetric shapes computed by the boundary integral method for an azimuthally averaged surface energy. We list as well the σ^* values corresponding to these shapes. Note that $\rho_p=\rho_{Iv}$ both for the paraboloid assumed in solvability theory and for the computed nonaxisymmetric and axisymmetric shapes, such that comparing σ_p^* values is equivalent here to comparing scaled velocity values $Vd_0/D=2\sigma_p^*P_{Iv}^2$. One remarkable fact is that the linear solvability theory predicts relatively accurately σ_p^* even though it does not describe the localized tip distortion that causes ρ to depart from ρ_p. Thus, we can conclude from this comparison that this distortion does not strongly affect the selection of the velocity. A reexamination of the phase-field results of Ref. [13] in terms of σ_p^* show, however, that the linear solvability theory becomes increasingly inaccurate for larger anisotropy values ($\epsilon_4>0.03$).

Finally, McFadden *et al.* [22] have recently carried out a perturbative analysis of the diffusion field around a nonaxisymmetric isothermal shape defined at leading order in A_4 by Eq. (2), where A_4 is treated as an expansion parameter. Since their analysis neglects capillary effects, their tip radius ρ should be compared to ρ_p here. They derived a correction to the Ivantsov relation [Eq. (1)] that can become significant in the limit of very low undercoolings. For the lowest undercooling studied here ($\Delta=0.1$), this correction is of the order of a percent and thus comparable to the accuracy at which ρ_p was determined numerically. Our results are therefore not in contradiction with their predictions. We note, however, that the universal nonisothermal shape found here starts to deviate from the isothermal one they consider only a short distance away from the tip where the fins develop under the action of anisotropic surface tension. Simulations at substantially lower undercooling would be necessary to test if this difference between the isothermal and nonisothermal shapes affects their predictions.

V. CONCLUSIONS

We have studied the three-dimensional morphology of the dendrite tip using recent improvements of the phase-field method [11–13] that make it possible to carry out quantitatively accurate simulations are relatively low undercoolings. Our main finding is that the experimentally measurable low undercooling tip morphology is independent of anisotropy strength and thus universal under the assumption that kinetic effects are negligible, in qualitative agreement with solvability theory [5,6]. The nonaxisymmetric deviation of this morphology from a paraboloid is well fitted by a single $\cos 4\phi$ mode with an amplitude that is about twice smaller than predicted by solvability theory and in good agreement with existing shape measurements in SCN [9]. Moreover, these measurements were reanalyzed here and found to be consistent with a nonaxisymmetric tip shape dominated by a single $\cos 4\phi$ mode as in our simulations.

The fins are well described away from the tip by the power law derived by Brener on the basis of the analogy [7] between three-dimensional steady-state shapes and two-dimensional time-dependent growth shapes [8], albeit with a slightly larger prefactor than predicted. Interestingly, the validity of this power law extends remarkably close to the tip. Our findings are also in good agreement with experimental data on xenon dendrites [10].

Finally, we conclude that the ''true'' tip radius is not an experimentally adequate parameter to characterize the tip operating state since the anisotropy-dependent shape distortion near the tip that fixes this radius is most likely not measurable. In contrast, the tip radius of the paraboloid which underlies the rest of the tip morphology (excluding this distortion) is both measurable and a good scaling parameter for the entire dendrite shape. The latter tip radius is indistinguishable from the Ivantsov prediction over the range of undercooling studied here, which does not exclude differences between these two radii to be present at even lower undercoolings [22].

It would be interesting in the future to extend the present study to investigate how the anisotropic kinetics of molecular attachment at the interface alters the tip morphology. The detailed study of the tip morphology, and in particular its departure from the universal shape characterized here, may actually provide a sensitive probe of interface kinetic effects.

ACKNOWLEDGMENTS

This research was supported by U.S. DOE Grant No. DE-FG02-92ER45471 and benefited from computer time allocation at the National Energy Resource Scientific Computing Center and the Northeastern University Advanced Scientific Computation Center. We thank Geoffrey McFadden for pointing out to us the analogy between the Wulff construction and the reconstruction of the dendrite shape from its projections.

[1] A. Papapetrou, Z. Kristallogr. **92**, 89 (1935).
[2] G. P. Ivantsov, Dokl. Akad. Nauk SSSR **58**, 567 (1947).
[3] J. S. Langer, in *Chance and Matter*, Lectures on the Theory of Pattern Formation, Les Houches, Session XLVI, edited by J. Souletie, J. Vannimenus, and R. Stora (North-Holland, Amsterdam, 1987), pp. 629–711.
[4] D. Kessler, J. Koplik, and H. Levine, Adv. Phys. **37**, 255 (1988).
[5] M. Ben Amar and E. Brener, Phys. Rev. Lett. **71**, 589 (1993).
[6] E. Brener and V. I. Melnikov, JETP **80**, 341 (1995).
[7] E. Brener, Phys. Rev. Lett. **71**, 3653 (1993).
[8] R. Almgren, W. S. Dai, and V. Hakim, Phys. Rev. Lett. **71**, 3461 (1993).
[9] J. C. LaCombe, M. B. Koss, V. E. Fradkov, and M. E. Glicksman, Phys. Rev. E **52**, 2778 (1995).
[10] U. Bisang and J. H. Bilgram, Phys. Rev. Lett. **21**, 3898 (1995); Phys. Rev. E **54**, 5309 (1996).
[11] M. Plapp and A. Karma, cond-mat/9906370, 1999.
[12] M. Plapp and A. Karma, Phys. Rev. Lett. (to be published).
[13] A. Karma and W.-J. Rappel, Phys. Rev. Lett. **77**, 4050 (1996); Phys. Rev. E **57**, 4323 (1998).
[14] J. S. Langer, in *Directions in Condensed Matter*, edited by G. Grinstein and G. Mazenko (World Scientific, Singapore, 1986), p. 164.
[15] J. B. Collins and H. Levine, Phys. Rev. B **31**, 6119 (1985).
[16] D. A. Kessler and H. Levine, Acta Metall. **36**, 2693 (1988).
[17] G. B. McFadden (private communications).
[18] D. P. Woodruff, *The Solid-Liquid Interface* (Cambridge University Press, London, 1973).
[19] J. W. Cahn and D. W. Hoffman, Acta Metall. **22**, 1205 (1974).
[20] M. Muschol, D. Liu, and H. Z. Cummins, Phys. Rev. A **46**, 1038 (1992).
[21] M. E. Glicksman and N. B. Singh, J. Cryst. Growth **98**, 277 (1989).
[22] G. B. McFadden, S. R. Coriell, and R. F. Sekerka, J. Cryst. Growth **208**, 726 (2000).
[23] A. Barbieri and J. S. Langer, Phys. Rev. A **39**, 5314 (1989).